SCIENCE CHINA Materials ARTICLES

mater.scichina.com link.springer.com

Published online 15 October 2020 | https://doi.org/10.1007/s40843-020-1453-0
Sci China Mater 2021, 64(3): 673–682

Tunable magnetism in layered $CoPS_3$ by pressure and carrier doping

Yue Gu, Shuqing Zhang and Xiaolong Zou*

ABSTRACT **Despite extensive research on recently discovered layered ferromagnetic (FM) materials, their further development is hampered by the limited number of candidate materials with desired properties. As a much bigger family, layered antiferromagnetic (AFM) materials represent excellent platforms to not only deepen our understanding of fundamental physics but also push forward high-performance spintronics applications. Here, by systematic first-principles calculations, we demonstrate pressure and carrier doping control of magnetic properties in layered AFM $CoPS_3$, a representative of transition metal phosphorus trichalcogenides. In particular, pressure can drive isostructural Mott transition, in sharp contrast to other transition metal thiophosphates. Intriguingly, both pressure and carrier doping can realize the long-sought FM half-metallic states with 100% spin polarization percentage, which is good for improving the injection and detection efficiency of spin currents among others. Moreover, the Mott transition is accompanied by instantaneous spin-crossover (SCO) in $CoPS_3$, and such cooperative SCO facilitates the implementation of fast-response reversible devices, such as data storage devices, optical displays and sensors. We further provide an in-depth analysis for the mechanisms of FM half-metallicity and SCO. Tunable magnetism in layered AFM materials opens vast opportunities for purposeful device design with various functionalities.**

Keywords: layered magnetic materials, magnetic transition, spin-crossover, half-metallic, first-principles calculations

INTRODUCTION

Layered magnetic materials have received a lot of research interest recently, due to their novel fundamental physics and broad application prospects [1–3]. In 2017, long-range magnetic order has been discovered in layered $Cr_2Ge_2Te_6$ and CrI_3 down to monolayer limit, which serve as ideal systems to study two-dimensional (2D) magnetic models [4,5]. While $Cr_2Ge_2Te_6$ is shown to be a two-dimensional (2D) Heisenberg ferromagnet, monolayer CrI_3 is an Ising ferromagnet, with antiferromagnetic (AFM) interlayer coupling in bilayers. Later, itinerant ferromagnetism was observed in Fe_3GeTe_2, with much elevated Curie temperature (T_c) [6]. These results have further ignited the enthusiasm of researchers to extensively search for other magnetic materials, including half-metals [7–17], half-semiconductors [18–20], bipolar magnets [21], etc. [22].

One of the outstanding features of layered magnetic materials is that their magnetic properties can be feasibly controlled by a large variety of external stimuli, especially easy-to-implement mechanical and electrical means. In CrI_3, a pressure about 2 GPa can induce stacking rearrangement, leading to an AFM-to-ferromagnetic (FM) transition [23,24]. Meanwhile, the T_c could be increased along with the change in magnetocrystalline anisotropy energy (MAE) [25]. The amount of MAE change in $Cr_2Ge_2Te_6$ can even reach 100% under a pressure of >1 GPa, leading to a switch from uniaxial to easy-plane anisotropy in magnetization [26]. For Fe_3GeTe_2, the compression results in the suppression of both T_c and magnetic moment, and thus the anomalous Hall conductivity [27,28]. Besides, the application of pressure can also cause spin-crossover (SCO) [29], which is an interesting magnetic phenomenon where spin states can change between high-spin (HS) and low-spin (LS) ones. This magnetic transition has excellent application potential in many aspects, such as fast-response switches [30,31], data storage devices [32], optical displays [33,34], and sensors [35].

Electrode gating is another practical and efficient route for controlling magnetism properties. Since electrostatic doping can alter the saturation magnetization, coercive force and T_c in monolayer CrI_3 [36], both doping and

Shenzhen Geim Graphene Center and Low-Dimensional Materials and Devices Laboratory, Tsinghua-Berkeley Shenzhen Institute (TBSI), Tsinghua University, Shenzhen 518055, China
* Corresponding author (email: xlzou@sz.tsinghua.edu.cn)

electric field lead to an AFM-FM transition in bilayer CrI_3 [36–38]. Bipolar gate-controlled magnetism can also be realized in $Cr_2Ge_2Te_6$, through the tuning of Fermi level and the resulting rebalance of spin-polarized electronic structure [39]. For Fe_3GeTe_2, ionic gating can significantly raise the T_c to near room-temperature [6].

As a representative family of layered materials, transition metal phosphorus trichalcogenides MPX_3 (M = Fe, Mn, Co and Ni; X = S and Se) share many intriguing structural and magnetic phase transition-related phenomena [40,41]. For instance, both experimental and theoretical studies have shown pressure can change the stacking sequence and magnetic order of $FePS_3$ [42,43]. Moreover, nearly instantaneous pressure-driven SCO has been discovered in MPX_3 (M = Mn, Fe; X = S, Se) [44,45]. For $FePSe_3$, superconductivity can emerge with a transition temperature about 3–5 K along with vanishing magnetic moments, which demonstrates a pursuit for superconductors in transition-metal-based hexagonal systems, useful for the understanding in the mechanism of high-temperature superconductivity [44]. For $MnPS_3$, an intriguing linear magnetoelectric phase was found, which originates from the broken time-reversal and spatial-inversion symmetries in Neel-AFM state [46]. Here, using first-principles calculations, we show that multiple structural and/or magnetic transitions can be induced in $CoPS_3$ by applying pressure or carrier doping, both of which can be easily implemented in experiments. Under an external pressure about 2 GPa, $CoPS_3$ changes from AFM bilayer-I (B-I) phase to AFM trilayer-I (T-I) phase. At about 12 GPa, it changes to FM half-metallic T-I phase accompanied with a cell volume collapse about 5% and an HS to LS crossover. Further increase of pressure above 19 GPa leads to FM metallic bilayer-II (B-II) phase. Also, various magnetic phase transitions happen under carrier doping. Both electron and hole doping in monolayer as well as hole doping in bulk $CoPS_3$ can induce an AFM to half-metallic FM transition. These results open abundant opportunities for using layered materials for spintronics devices with easy-to-control pressure and doping tuning.

METHODS

All simulastions were performed using Vienna *ab initio* simulation package (VASP) [47,48]. The exchange-correlation was described by Perdew-Burke-Ernzerhof version of the generalized gradient approximation (GGA) [49], and the ion-electron interaction was included using the projector augmented wave (PAW) method [50]. The cutoff energy for plane waves was set to 500 eV. The density functional DFT-D3 method was used to take into account the Van der Waals interactions [51]. The structural relaxation was performed till the force of every atom was smaller than 0.01 eV $Å^{-1}$, and the energy was converged to 1×10^{-5} eV. These settings make the simulated structure closely match those from experiments. The calculated cell parameters for bulk $CoPS_3$ without external pressure are 5.90 Å×10.24 Å×6.67 Å, while experimental result is 5.90 Å×10.19 Å×6.60 Å at 160 K [52]. The onsite Coulomb interaction of 3d orbitals of Co was simulated by the DFT+U method [53] with U for Co set to 3.3. For B-I and B-II phases, supercells containing 40 atoms were used. While supercells containing 120 atoms were used for the T-I phase. The spin-orbit coupling was also considered for their influences on magnetic anisotropy and band structures. Carrier doping was achieved by changing the number of electrons, and a homogeneous background charge was introduced to neutralize the considered systems.

RESULTS AND DISCUSSION

Magnetic states controlled by pressure

The transition metal phosphorus trichalcogenides MPX_3 (M = Fe, Mn, Co and Ni; X = S and Se) are layered compounds with 2D monolayers bound by van der Waals force. The monolayer is composed of MX_6 octahedra forming a honeycomb lattice, and the center of the transition metal hexagons is occupied by P-P dimers (see Fig. S1). For the structures of MPS_3, the space group is $C2/m$, and the monolayers are stacked with inclined AA sequence, as indicated by Fig. 1a. While for $MPSe_3$ expect $NiPSe_3$ with $C2/m$ symmetry, the space group is $R\bar{3}$, and the stacking sequence of monolayers is ABCABC, as shown in Fig. 1b. In addition to these two phases, experimental and theoretical studies [42,43] have found new high-pressure phase in $FePX_3$, which has the similar intralayer structure but exhibits AA stacking sequence, shown in Fig. 1c with $C2/m$ space group. Here, we name these three structures as B-I, T-I, and B-II phases, respectively.

Besides the change of the structural phases, layered MPX_3 often undergo various magnetic order transitions under pressure. Fig. 2a shows four possible magnetic orders of transition metal ions in MPX_3, including FM and three AFM orders: Stripy-AFM (sAFM), Neel-AFM (nAFM), and Zigzag-AFM (zAFM). When the magnetic moments of transition metal ions in adjacent layers are coupled antiferromagnetically, four more magnetic orders emerge, labelled as FM′, sAFM′, nAFM′ and zAFM′

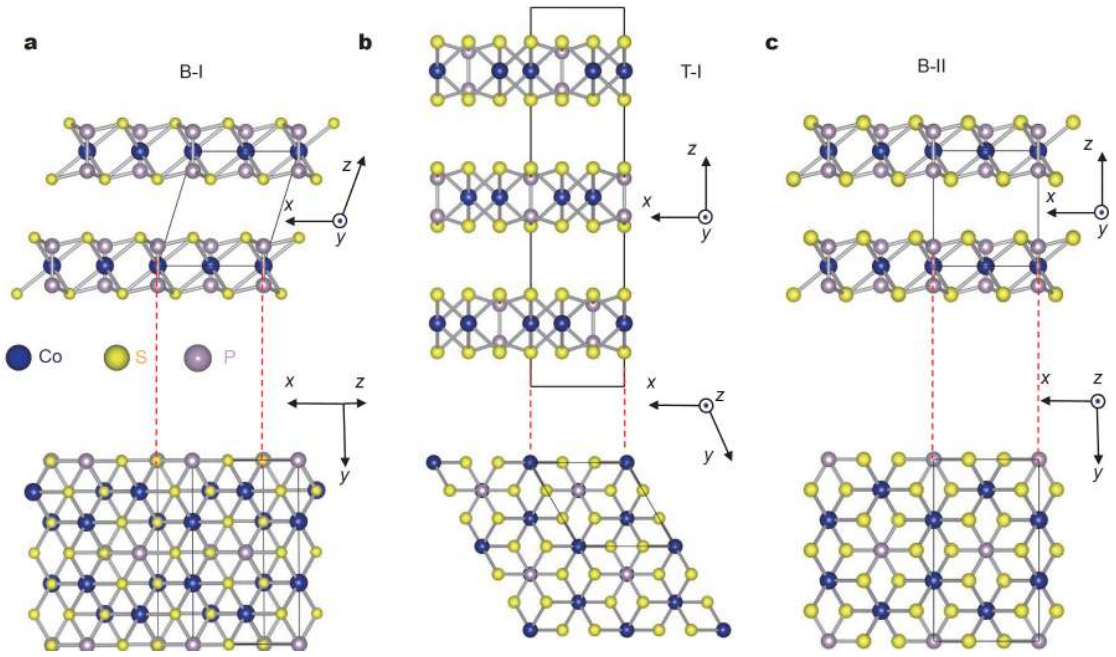

Figure 1 Crystal structures for $CoPS_3$. Side (upper panels) and top views (bottom panels) of (a) B-I, (b) T-I and (c) B-II phases.

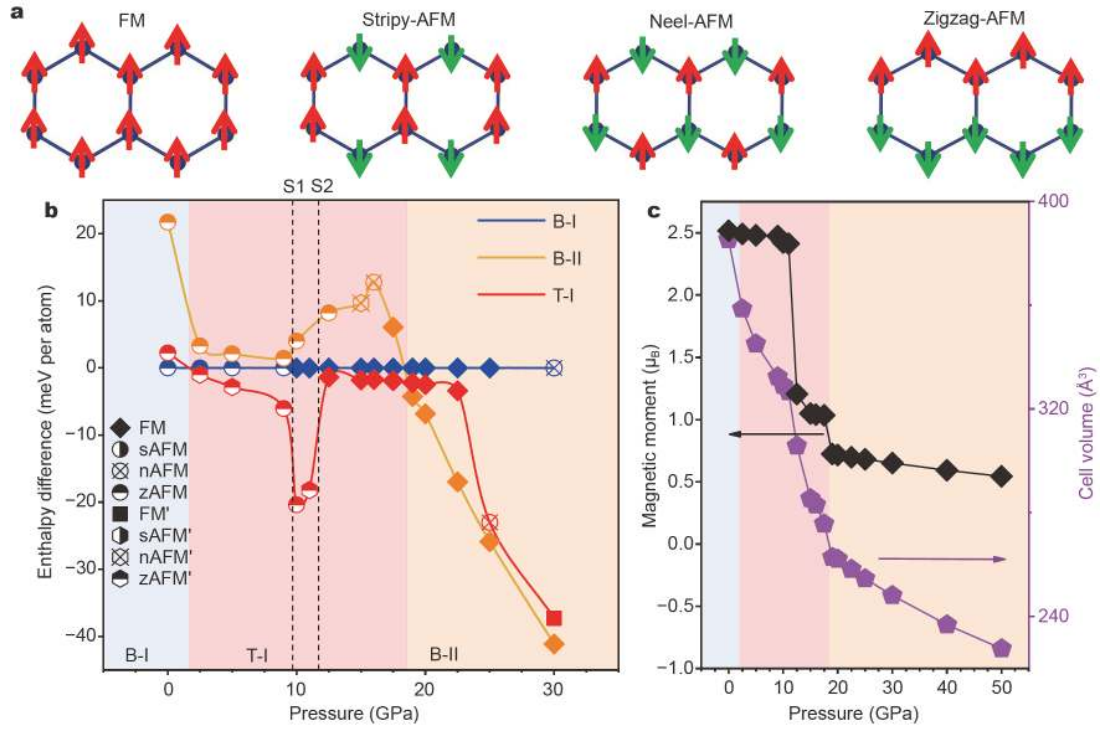

Figure 2 (a) FM and three AFM orders: Stripy-AFM (sAFM), Neel-AFM (nAFM), and Zigzag-AFM (zAFM). (b) The energy difference of $CoPS_3$ with different phases as a function of pressure, and the energy of B-I phase is set as zero. Different magnetic orders are indicated by different symbols in the inset, and only the lowest energy of various magnetic orders is shown for each phase. The dashed lines S1 and S2 correspond to the pressures of SCO of B-I and T-I phases, respectively. (c) Magnetic moments of Co^{2+} ions and the cell volume (for a cell with 20 atoms) in ground-state $CoPS_3$ as functions of pressure.

(see Fig. S2) with their intralayer magnetic configurations the same as FM, sAFM, nAFM and zAFM. Based on the above three structural phases and eight magnetic orders, we systematically explored the variation of structural and magnetic phases of $CoPS_3$ under different pressures.

First of all, in the absence of external pressure, the ground-state phase of $CoPS_3$ is zAFM B-I. Due to the Co^{2+} d^7 configuration with orbital triplet ground state, the spin-orbit coupling (SOC) will play a role in its magnetic interaction, in particular the anistropy. The calculated energies for zAFM states with the magnetic moment along different axes show the easy magnetization axis is along the *x* direction in the plane (see Table S1), and the orbital moments of about 0.2 μ_B also prefer to align in the *x* direction. The obtained magnetic ground-state order and the easy magnetization axis are well consistent with previous experimental work [52]. However, it should be noted the energy difference caused by SOC is only about 0.5 meV/atom, which is much less than those arised from the structural phase transitions discussed below. Meanwhile, the SOC is ineffective in LS states under high pressure. Therefore, we ignored the SOC effect in the following calculations on structrual transition, and the influences of SOC on electronic band structures are provided in Fig. S3.

Next, in order to study structural phase transition under pressure, the energies of T-I and B-II phases as a function of pressure are displayed in Fig. 2b, taking the lowest energy of B-I phase as reference. Here, only the lowest energy of eight magnetic orders for each phase is shown, with the detailed variations of energies for eight magnetic orders for three different structural phases shown in Fig. S4. The variation of structural phases can be clearly divided into three stages. First, when the pressure is low, the ground-state phase remains at zAFM B-I. At a critical pressure about 2 GPa, the ground-state changes to zAFM′ T-I phase. In the range from 2 to 12.5 GPa, the magnetic state of T-I phase undergoes multiple transitions among zAFM and zAFM′, indicating the delicate competition between FM and AFM interlayer coupling. Interestingly, at about 12.5 GPa, $CoPS_3$ experiences an AFM to FM transition while the structural phase keeps at T-I. Then it retains at FM T-I phase until the pressure reaches about 19 GPa and beyond, where FM B-II phase becomes the most stable one. It should be mentioned a high-pressure B-III phase, which has $P\bar{3}1m$ symmetry and the same stacking sequence as B-II as observed in $FePS_3$, is always higher in energy than B-II phase.

Along with the variation of structural and magnetic phases under different pressures, the magnetic moments for Co^{2+} ions also change significantly. As shown in Fig. 2c, the local magnetic moments of Co^{2+} ions change from ~2.5 to ~1 μ_B at a critical pressure about 12 GPa, which suggests a transition from HS to LS states, showing clear SCO phenomenon. The pressure at which SCO occurs corresponds exactly to where the magnetic order changes from AFM to FM in the T-I phase. After 12 GPa, the magnetic moments slowly decrease, and show another small sudden change from ~1 to ~0.7 μ_B at 19 GPa, which corresponds to the phase transition from T-I to B-II phases. Finally, the magnetic moments slowly decrease to ~0.5 μ_B. Since the effective ionic radii of HS and LS Co^{2+} ions are notably different (0.75 Å *versus* 0.65 Å) [54], the transition from HS to LS states results in a significant reduction in Co–S bond lengths and thus the cell parameters. Fig. 2c also shows the variation of cell volume of $CoPS_3$, and there is a small volume collapse of about 5% from 11.5 to 12 GPa. It is worth noting that for both B-I and B-II phases, the SCO occurs at about 10 GPa (line S1 in Fig. 2b). Nevertheless, since the T-I phase is the most stable one in a wide range from 2 to 19 GPa, the overall SCO appears at about 12 GPa (line S2 in Fig. 2b). In the range between line S1 and S2, only Co^{2+} ions of T-I phase show HS state, which may be the cause of the deep valley for the energy profile of T-I phase in Fig. 2b. In short, $CoPS_3$ under pressure undergoes the transition from AFM B-I to AFM T-I, then to FM T-I and finally to FM B-II phase with distinctly different magnetic properties.

Some comparison with other MPX_3 compounds can be made. For $FePS_3$, previous work [42,43] shows that its structure transforms from B-I to B-II phases at about 5 GPa, while the magnetic orders of these two phases are both zAFM. Differently, in $CoPS_3$, the most stable phase is the T-I phase in a wide pressure range (about 2–19 GPa), which exhibits the same stacking sequence as the ground-state phases of $MPSe_3$. In addition, the value of volume collapse in $CoPS_3$ is much smaller than the experimental results for $FePS_3/Se_3$ (~10%) [44]. It is because the effective ionic radii of HS and LS Fe^{2+} ions are 0.78 and 0.61 Å, the difference of which is much larger than that of Co^{2+} ions. More importantly, when the pressure is larger than 12.5 GPa, the $CoPS_3$ in either T-I or B-II phase is FM, and the magnetic moments of Co^{2+} ions do not disappear even until 50 GPa. While for $FePS_3$, the magnetic moments of Fe^{2+} ions disappear and the system becomes nonmagnetic when the pressure is larger than 17 GPa. The much more robust magnetic behaviors of $CoPS_3$ under high pressure probably originate from the odd-numbered (seven) of 3d electrons of Co^{2+} ions in-

stead of the six 3d electrons of Fe^{2+}. The extra unpaired electron has important consequences on the electronic structure, as discussed below.

Electronic structures under different pressures and its transition mechanism

To see the influences of different structural phases and magnetic orders on the electronic properties, Fig. 3 shows typical band structures and projected density of states (PDOS) for the ground states of $CoPS_3$ under different pressures. At 0 GPa, $CoPS_3$ is in zAFM B-I phase with a significant band gap about 1.53 eV, and its energy bands experiences notable SOC splitting, as shown in Fig. S3a. For T-I phase under low pressure before the SCO occurs, it remains an AFM semiconductor with a large band gap. The band structure for zAFM T-I phase at 10 GPa is displayed in Fig. 3b showing a band gap about 1.28 eV. When SCO happens at high pressure, the most stable phase changes to FM T-I phase in the range from 12.5 to 19 GPa, with a representative band structure at 15 GPa shown in Fig. 3c. Interestingly, the FM state is half-metallic with the Fermi level intersecting spin-up bands, while the bandgap arises for the spin-down bands, giving rise to 100% spin polarization percentage around the Fermi level. When the pressure is larger than 19 GPa, the ground state becomes FM B-II phase with metallic behavior. These transition behaviors are distinctly different from extensively studied $FePS_3$ [43], where the Mott insulator-metal transition in $FePS_3$ happens between B-II and B-III phases. In contrast, the transition in $CoPS_3$ is isostructural in T-I phase, which is similar to $V_{0.9}PS_3$ [55]. Based on the above analysis, this continuous transition among various magnetic states in $CoPS_3$, from AFM semiconductor to FM half-metal and then to FM metal during the gradual pressurization process, should bring more possibilities to its applications.

Among various magnetic states, half metal is a particularly interesting one, because its high spin polarization percentage in low energy is advantageous for various spintronics applications, for example, the enhancement in the efficiency of the injection and detection of spin currents. Half-metal gap is a key parameter determining its robustness, and is defined as the minimum of two energy differences, E_{HMG}= MIN{E_1, E_2} with E_1 and E_2 schematically defined in Fig. 3c. The obtained half-metal gaps of $CoPS_3$ at 12, 15, 17.5 GPa are 0.63, 0.65 and 0.67 eV, respectively. These half-metal gaps are much larger compared with thermal energy at room temperature,

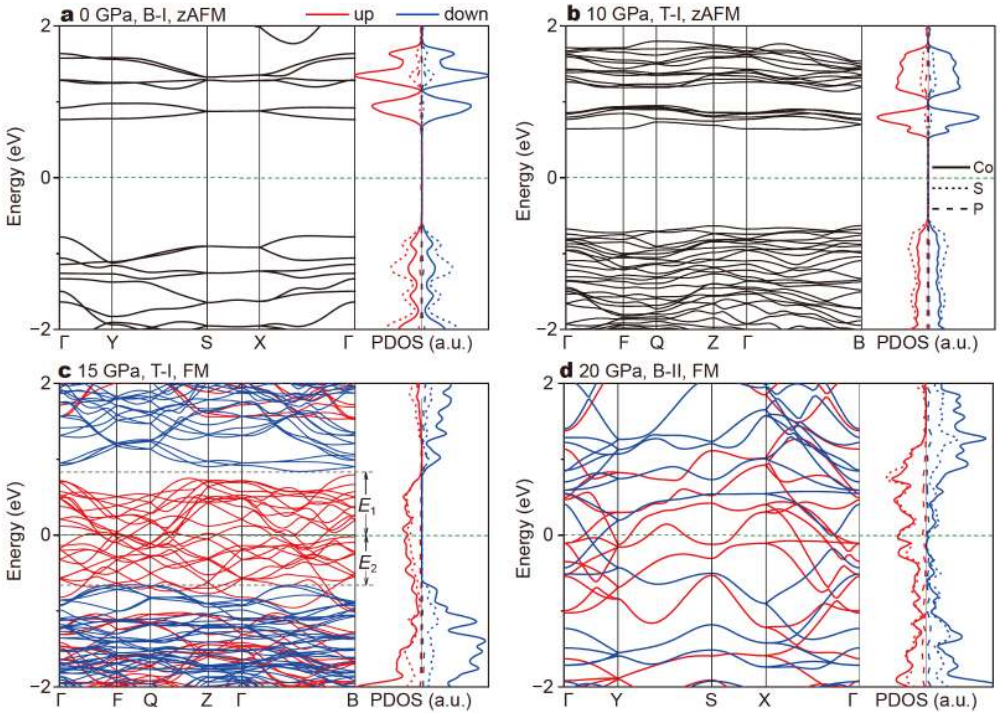

Figure 3 Electronic band structures and projected density of states (PDOS) of ground states under different pressures (a) 0 GPa, zAFM B-I phase; (b) 10 GPa, zAFM T-I phase; (c) 15 Pa, FM T-I phase; (d) 20 GPa, FM B-II phase. Blue and red lines represent spin-up and spin-down channels, respectively, while solid, dotted and dashed lines represent the PDOS of Co, S and P, respectively.

guaranteeing the stability of half-metallicity under practical conditions. We also estimated the T_c of $CoPS_3$ with FM half-metallicity by mean-field theory (MFT). The highest T_c can even be higher than 330 K after considering the overestimation from MFT [9], indicating the pressure-induced FM half-metallicity can exist above room temperature (details are shown in Fig. S6 and Table S5). It should be mentioned, as the pressure is larger than 12.5 GPa, the interlayer nearest-neighbor Co–Co distance becomes smaller than the intralayer second-neighbor distance, shown in Table S2. It facilitates the semiconductor-metal transition and leads to an enhancement of interlayer exchange interaction, the latter of which suggests the effective dimensionality of exchange interaction increases significantly. Similar increase in the effective dimensionality of transport behaviors is observed in $V_{0.9}PS_3$ under high pressure [55]. The intriguing AFM to FM half-metallic transition could be in principle studied by refractive magnetic circular dichroism, magneto-optical Kerr effect microscopy, and transport measurement. Combined with structural characterization techniques, they will provide a wealth of information about magnetic properties for further investigation.

The emergence of the half-metallic FM state is closely related to the SCO, and an in-depth understanding of the SCO in $CoPS_3$ can be obtained by following the variations of the position and occupancy of five Co^{2+} 3d orbitals. Here, we take FM T-I phase as an example. Fig. S5 shows the schematic CoS_6 octahedron along with key structural parameters, and Table S3 lists the corresponding bond lengths and angles. The octahedral crystal field splits Co 3d orbitals into double-degenerate high-energy e_g levels (d_{z^2} and $d_{x^2-y^2}$ and triply-degenerate low-energy t_{2g} levels (d_{xy}, d_{yz}, and d_{xz}). These two groups of energy levels are separated by $\Delta_o = 10Dq$ [56], where $D = 35Ze^2/4a^5$ with Ze and a the charge of each ligand ion and the metal-ligand distance respectively, and $q = (2/105)\langle r^4\rangle$ with r the radial position of 3d electrons. Table S3 shows the bond lengths in CoS_6 octahedron are significantly shortened at 12 GPa, leading to a significant increase of Δ_o, which in turn causes the transition from the HS to LS states, following Hund's rule. Meanwhile, the CoS_6 octahedron is more severely distorted when the pressure reaches 12 GPa, which could lead to further splitting. Nevertheless, the split of orbitals inside e_g or t_{2g} level is not obvious, and can be appropriately regarded as degenerate orbitals.

When the pressure is near 12 GPa, the schematic PDOS diagrams of e_g and t_{2g} orbitals before and after SCO are shown in Fig. 4a. For lower pressure case, the spin-up e_g and spin-down t_{2g} orbitals split into bonding and anti-bonding states due to the metal-ligand interaction, while spin-down e_g and spin-up t_{2g} keep degenerate. When SCO occurs under higher pressure, the position of spin-up e_g and t_{2g} shifts up notably, as indicated by red symbols in Fig. 4b. And the position of the spin-down t_{2g} moves downward significantly, as indicated by blue rhombs. Consequently, both spin-up and spin-down t_{2g} orbitals become nearly fully occupied, shown by rhombs in Fig. 4c, consistent with Hund's rule-determined electronic configurations under enhanced crystal field splitting. The remaining one d electron of Co^{2+} ion occupies the spin-up e_g state, with significant increase of weight in anti-bonding states transferred from lower bonding states. Importantly, spin-up e_g becomes partially occupied, leading to half-metallic behavior. The Co^{2+} d^7 configuration tends to couple with others ferromagnetically through Co–S–Co superexchange interaction [9], following the Goodenough-Kanamori rules [57,58]. For comparison, in 2D transition-metal phosphides with tetragonal symmetry, the competition between d–d direct exchange and d–p–d super-exchange mechanisms leads to FM and AFM couplings in Co_2P and Fe_2P, respectively [59]. From Fig. 4b, we can also determine the exchange splitting for both e_g and t_{2g} orbitals, as well as the ligand-field splitting between e_g and t_{2g}. The dramatic change in the ligand field causes the upward shift of the position of e_g relative to that of t_{2g} (stars in Fig. 4d), while the exchange splitting decreases (black symbols), causing the quenching of magnetic moments, and thus the LS state.

Magnetic states controlled by carrier doping

Besides the application of pressure, carrier doping can also induce significant change in magnetic properties of layered $CoPS_3$. Fig. 5 shows the change of energies of various AFM states relative to FM state under carrier doping for both monolayer and bulk $CoPS_3$ structures. For monolayer, $CoPS_3$ maintains its zAFM ground state under a low amount of carrier doping. However, the energy of AFM state increases quickly compared to the FM one, suggesting carrier-induced destabilization of AFM state. At high carrier concentration, an AFM-FM transition occurs for electron doping at about 0.045e per atom and hole doping at about 0.028 h per atom. Meanwhile, for hole doping, the energy of sAFM relative to FM reaches the highest point at 0.02 h per atom, and then gradually decreases as the hole concentration increases. Its value becomes negative at about 0.05 h per atom, where a phase transition from FM to sAFM occurs. For electron doping, the relative energy value of zAFM

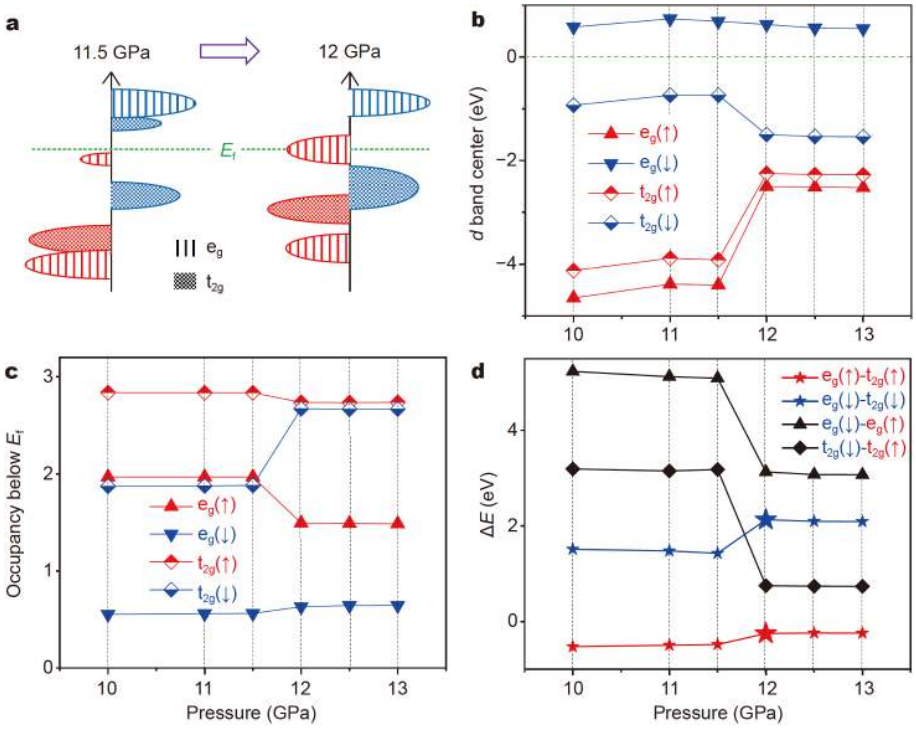

Figure 4 (a) Schematic PDOS diagrams of e_g and t_{2g} orbitals in $CoPS_3$ from 10 to 13 GPa, red for spin-up and blue for spin-down. (b) The d-band centers and (c) electronic occupancies below Fermi level of e_g and t_{2g} orbitals from 10 to 13 GPa. (d) The energy differences between different d-band centers in (b). Note the difference for e_g/t_{2g} orbitals in different channels represents the exchange splitting, while the different between e_g and t_{2g} orbitals in the same channel is proportional to crystal field splitting.

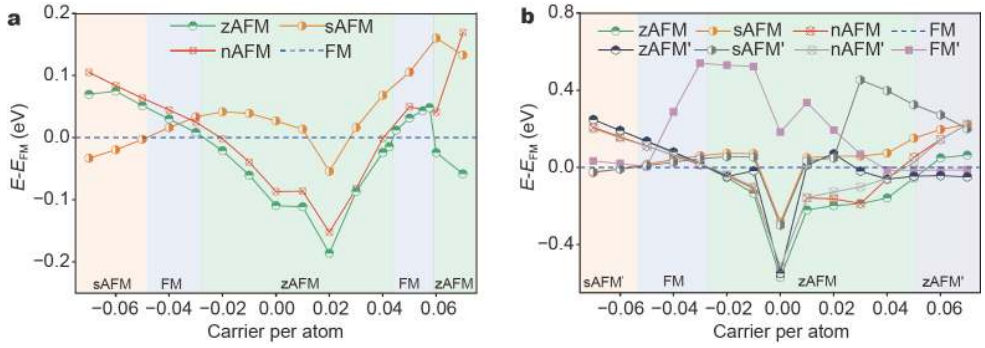

Figure 5 The variation of energies of different AFM states relative to FM state under carrier doping, for (a) monolayer and (b) bulk $CoPS_3$ structures. There are two layers of $CoPS_3$ in the bulk cell. The labels with superscript prime indicate magnetic states with AFM interlayer coupling, while those without prime represent magnetic states with FM interlayer coupling.

decreased to negative again at about 0.06e per atom, causing the magnetic ground state to change back to zAFM. The doping range of FM ground state corresponds approximately to 0.028–0.048 h per atom or 0.045–0.059e per atom. FM ground state can be achieved in a broader hole doping range with lower density by hole doping. We proceed to estimate the T_c in 0.04, 0.03 h and 0.05e per atom doping cases as about 80, 66 and 204 K, respectively. Moreover, for the monolayer case, the MAE is a key factor for the stabilization of 2D FM order. Table S4 shows the total energies of doped monolayer FM $CoPS_3$ with its magnetization direction along *x*, *y*, and *z* axes respectively. It can be found that the easy magnetization axis always remains in the plane. Interestingly, MAEs in the hole doping cases are about one order of magnitude larger than those of electron doping cases. Even for the

electron doping cases, the MAE about 1–10 meV f.u.$^{-1}$ is much larger compared with other 2D magnetic materials, such as 0.6 meV f.u.$^{-1}$ in $CoGa_2Te_4$ and 0.18 meV f.u.$^{-1}$ in MnB [9,60]. The underlying mechanism for such enhancement in MAE deserves further investigation.

For bulk $CoPS_3$, we further considered four magnetic orders with AFM interlayer coupling, i.e., FM′, sAFM′, nAFM′ and zAFM′ following the same labeling as above (Fig. S2). Overall, the phase transition shares similar characteristics as monolayer case. For hole doping, magnetic states with different interlayer couplings but the same intralayer spin configuration has similar energies, except that FM′ is much higher in energy than the FM one in most range. The change of magnetic ground state of bulk $CoPS_3$ with hole doping also shows a transition from zAFM to FM to sAFM, and the two critical concentrations are about 0.027 and 0.053 h per atom, respectively. On the other hand, for electron doping, the relative energy of zAFM state increases monotonously with increasing doping concentration and becomes positive at about 0.055e per atom. Meanwhile, the energy of zAFM′ decreases monotonously starting from about 0.02e per atom, and becomes lower than zAFM at about 0.05e per atom as new ground state. Compared with monolayer $CoPS_3$, the FM ground state of bulk $CoPS_3$ can only occur under hole doping, but its corresponding hole concentration range (0.027–0.053 h per atom) is slightly wider than that of monolayer (0.028–0.048 h per atom). The critical carrier concentrations for realizing AFM-to-FM transition are comparable to those reported for monolayer $MnPSe_3$ (0.011e / 0.013 h per atom) [10]. Interestingly, the FM state is also half-metallic (shown in Fig. S7), opening new possibilities for gate or doping controlled magnetic transition. The estimated T_c for hole-doped bulk $CoPS_3$ are about 119, 85 and 47 K at 0.05, 0.04 and 0.03 h per atom, respectively.

CONCLUSIONS

In summary, we predicted $CoPS_3$ could exhibit various structural and/or magnetic phase transitions through applying pressure or carrier doping. Under increasing pressure, the system undergoes phase transition from AFM B-I to AFM T-I, then to FM T-I and finally to FM B-II phase, accompanied by SCO behavior at about 12 GPa. When pressure is larger than about 12.5 GPa, FM $CoPS_3$ exhibits metallic properties. Especially in the range from 12.5 to 19 GPa, FM T-I phase exhibits half-metallic behaviors. Similarly, carrier doping can induce various magnetic transition. Importantly, both electron and hole doping in monolayer $CoPS_3$ as well as hole doping in bulk $CoPS_3$ can result in an AFM to half-metallic FM transition. The range of doping concentration for realizing FM ground state in monolayer $CoPS_3$ is about 0.028–0.048 h or 0.045–0.059e per atom, while that for hole doping in bulk $CoPS_3$ is about 0.027–0.053 h per atom, all of which are achievable under experimental conditions. The predicted multiple structural and magnetic phase transition, FM (half-)metallic states, and SCO behavior in layered $CoPS_3$ suggest its great potentials for diverse new-generation spintronics applications.

Received 1 June 2020; accepted 2 July 2020; published online 15 October 2020

1 Gong C, Zhang X. Two-dimensional magnetic crystals and emergent heterostructure devices. Science, 2019, 363: eaav4450
2 Xu R, Zou X, Liu B, *et al.* Computational design and property predictions for two-dimensional nanostructures. Mater Today, 2018, 21: 391–418
3 Zhang Z, Liu X, Yu J, *et al.* Tunable electronic and magnetic properties of two-dimensional materials and their one-dimensional derivatives. WIREs Comput Mol Sci, 2016, 6: 324–350
4 Gong C, Li L, Li Z, *et al.* Discovery of intrinsic ferromagnetism in two-dimensional van der Waals crystals. Nature, 2017, 546: 265–269
5 Huang B, Clark G, Navarro-Moratalla E, *et al.* Layer-dependent ferromagnetism in a van der Waals crystal down to the monolayer limit. Nature, 2017, 546: 270–273
6 Deng Y, Yu Y, Song Y, *et al.* Gate-tunable room-temperature ferromagnetism in two-dimensional Fe_3GeTe_2. Nature, 2018, 563: 94–99
7 Ashton M, Gluhovic D, Sinnott SB, *et al.* Two-dimensional intrinsic half-metals with large spin gaps. Nano Lett, 2017, 17: 5251–5257
8 Sun Q, Kioussis N. Prediction of manganese trihalides as two-dimensional Dirac half-metals. Phys Rev B, 2018, 97: 094408
9 Zhang S, Xu R, Duan W, *et al.* Intrinsic half-metallicity in 2D ternary chalcogenides with high critical temperature and controllable magnetization direction. Adv Funct Mater, 2019, 29: 1808380
10 Li X, Wu X, Yang J. Half-metallicity in $MnPSe_3$ exfoliated nanosheet with carrier doping. J Am Chem Soc, 2014, 136: 11065–11069
11 Li X, Wu X, Yang J. Room-temperature half-metallicity in La(Mn, Zn)AsO alloy *via* element substitutions. J Am Chem Soc, 2014, 136: 5664–5669
12 Xu R, Liu B, Zou X, *et al.* Half-metallicity in Co-doped WSe_2 nanoribbons. ACS Appl Mater Interfaces, 2017, 9: 38796–38801
13 Kan E, Li Z, Yang J, *et al.* Half-metallicity in edge-modified zigzag graphene nanoribbons. J Am Chem Soc, 2008, 130: 4224–4225
14 Li Y, Zhou Z, Shen P, *et al.* Spin gapless semiconductor-metal-half-metal properties in nitrogen-doped zigzag graphene nanoribbons. ACS Nano, 2009, 3: 1952–1958
15 Wang SS, Yu ZM, Liu Y, *et al.* Two-dimensional nodal-loop half-metal in monolayer MnN. Phys Rev Mater, 2019, 3: 084201
16 Liu Z, Liu J, Zhao J. YN_2 monolayer: Novel p-state Dirac half metal for high-speed spintronics. Nano Res, 2017, 10: 1972–1979
17 Xuan X, Guo W, Zhang Z. Surface multiferroics in silicon enabled

by hole-carrier doping. Sci Bull, 2019, 64: 331–336
18 Zhang WB, Qu Q, Zhu P, *et al.* Robust intrinsic ferromagnetism and half semiconductivity in stable two-dimensional single-layer chromium trihalides. J Mater Chem C, 2015, 3: 12457–12468
19 Wu Z, Yu J, Yuan S. Strain-tunable magnetic and electronic properties of monolayer CrI_3. Phys Chem Chem Phys, 2019, 21: 7750–7755
20 Guo Y, Wang B, Zhang X, *et al.* Magnetic two-dimensional layered crystals meet with ferromagnetic semiconductors. InfoMat, 2020, 2: 639–655
21 Li X, Yang J. Bipolar magnetic materials for electrical manipulation of spin-polarization orientation. Phys Chem Chem Phys, 2013, 15: 15793–15801
22 Yang H, Pan L, Xiao M, *et al.* Iron-doping induced multiferroic in two-dimensional In_2Se_3. Sci China Mater, 2020, 63: 421–428
23 Li T, Jiang S, Sivadas N, *et al.* Pressure-controlled interlayer magnetism in atomically thin CrI_3. Nat Mater, 2019, 18: 1303–1308
24 Song T, Fei Z, Yankowitz M, *et al.* Switching 2D magnetic states *via* pressure tuning of layer stacking. Nat Mater, 2019, 18: 1298–1302
25 Mondal S, Kannan M, Das M, *et al.* Effect of hydrostatic pressure on ferromagnetism in two-dimensional CrI_3. Phys Rev B, 2019, 99: 180407
26 Lin Z, Lohmann M, Ali ZA, *et al.* Pressure-induced spin reorientation transition in layered ferromagnetic insulator $Cr_2Ge_2Te_6$. Phys Rev Mater, 2018, 2: 051004
27 Wang X, Li Z, Zhang M, *et al.* Pressure-induced modification of the anomalous Hall effect in layered Fe_3GeTe_2. Phys Rev B, 2019, 100: 014407
28 Wang H, Xu R, Liu C, *et al.* Pressure-dependent intermediate magnetic phase in thin Fe_3GeTe_2 flakes. J Phys Chem Lett, 2020, 11: 7313–7319
29 Wang Y, Bai L, Wen T, *et al.* Giant pressure-driven lattice collapse coupled with intermetallic bonding and spin-state transition in manganese chalcogenides. Angew Chem Int Ed, 2016, 55: 10350–10353
30 Decurtins S, Gütlich P, Köhler CP, *et al.* Light-induced excited spin state trapping in a transition-metal complex: The hexa-1-propyltetrazole-iron (II) tetrafluoroborate spin-crossover system. Chem Phys Lett, 1984, 105: 1–4
31 Ohkoshi SI, Imoto K, Tsunobuchi Y, *et al.* Light-induced spin-crossover magnet. Nat Chem, 2011, 3: 564–569
32 Kahn O, Martinez CJ. Spin-transition polymers: From molecular materials toward memory devices. Science, 1998, 279: 44–48
33 Bonhommeau S, Molnár G, Galet A, *et al.* One shot laser pulse induced reversible spin transition in the spin-crossover complex $[Fe(C_4H_4N_2)\{Pt(CN)_4\}]$ at room temperature. Angew Chem Int Ed, 2005, 44: 4069–4073
34 Kahn O, Kröber J, Jay C. Spin transition molecular materials for displays and data recording. Adv Mater, 1992, 4: 718–728
35 Halder GJ, Kepert CJ, Moubaraki B, *et al.* Guest-dependent spin crossover in a nanoporous molecular framework material. Science, 2002, 298: 1762–1765
36 Jiang S, Li L, Wang Z, *et al.* Controlling magnetism in 2D CrI_3 by electrostatic doping. Nat Nanotech, 2018, 13: 549–553
37 Huang B, Clark G, Klein DR, *et al.* Electrical control of 2D magnetism in bilayer CrI_3. Nat Nanotech, 2018, 13: 544–548
38 Xu R, Zou X. Electric field-modulated magnetic phase transition in van der Waals CrI_3 bilayers. J Phys Chem Lett, 2020, 11: 3152–3158
39 Wang Z, Zhang T, Ding M, *et al.* Electric-field control of magnetism in a few-layered van der Waals ferromagnetic semiconductor. Nat Nanotech, 2018, 13: 554–559
40 Le Flem G, Brec R, Ouvard G, *et al.* Magnetic interactions in the layer compounds MPX_3 (M = Mn, Fe, Ni; X = S, Se). J Phys Chem Solids, 1982, 43: 455–461
41 Chittari BL, Park Y, Lee D, *et al.* Electronic and magnetic properties of single-layer MPX3 metal phosphorous trichalcogenides. Phys Rev B, 2016, 94: 184428
42 Haines CRS, Coak MJ, Wildes AR, *et al.* Pressure-induced electronic and structural phase evolution in the van der Waals compound $FePS_3$. Phys Rev Lett, 2018, 121: 266801
43 Zheng Y, Jiang X, Xue X, *et al. Ab initio* study of pressure-driven phase transition in $FePS_3$ and $FePSe_3$. Phys Rev B, 2019, 100: 174102
44 Wang Y, Ying J, Zhou Z, *et al.* Emergent superconductivity in an iron-based honeycomb lattice initiated by pressure-driven spin-crossover. Nat Commun, 2018, 9: 1914
45 Wang Y, Zhou Z, Wen T, *et al.* Pressure-driven cooperative spin-crossover, large-volume collapse, and semiconductor-to-metal transition in manganese (II) honeycomb lattices. J Am Chem Soc, 2016, 138: 15751–15757
46 Chu H, Roh CJ, Island JO, *et al.* Linear magnetoelectric phase in ultrathin $FePS_3$ probed by optical second harmonic generation. Phys Rev Lett, 2020, 124: 027601
47 Kresse G, Furthmüller J. Efficiency of *ab-initio* total energy calculations for metals and semiconductors using a plane-wave basis set. Comput Mater Sci, 1996, 6: 15–50
48 Kresse G, Furthmüller J. Efficient iterative schemes for *ab initio* total-energy calculations using a plane-wave basis set. Phys Rev B, 1996, 54: 11169–11186
49 Perdew JP, Burke K, Ernzerhof M. Generalized gradient approximation made simple. Phys Rev Lett, 1996, 77: 3865–3868
50 Kresse G, Joubert D. From ultrasoft pseudopotentials to the projector augmented-wave method. Phys Rev B, 1999, 59: 1758–1775
51 Grimme S, Antony J, Ehrlich S, *et al.* A consistent and accurate *ab initio* parametrization of density functional dispersion correction (DFT-D) for the 94 elements H-Pu. J Chem Phys, 2010, 132: 154104
52 Wildes AR, Simonet V, Ressouche E, *et al.* The magnetic properties and structure of the quasi-two-dimensional antiferromagnet $CoPS_3$. J Phys-Condens Matter, 2017, 29: 455801
53 Anisimov VI, Zaanen J, Andersen OK. Band theory and Mott insulators: Hubbard *U* instead of Stoner *I*. Phys Rev B, 1991, 44: 943–954
54 Shannon RD. Revised effective ionic radii and systematic studies of interatomic distances in halides and chalcogenides. Acta Crystallogr Sect A, 1976, 32: 751–767
55 Coak MJ, Son S, Daisenberger D, *et al.* Isostructural Mott transition in 2D honeycomb antiferromagnet $V_{0.9}PS_3$. npj Quantum Mater, 2019, 4: 38
56 Sugano S, Tanabe Y, Kayamimura H. Multiplets of Transition-Metal Ions in Crystals. New York: Academic Press, 1970
57 Kanamori J. Superexchange interaction and symmetry properties of electron orbitals. J Phys Chem Solids, 1959, 10: 87–98
58 Goodenough JB. Magnetism and Chemical Bond. Genèva: Interscience Publishers, 1963
59 Liu Q, Xing J, Jiang Z, *et al.* 2D tetragonal transition-metal phosphides: An ideal platform to screen metal shrouded crystals for multifunctional applications. Nanoscale, 2020, 12: 6776–6784
60 Jiang Z, Wang P, Jiang X, *et al.* MBene (MnB): A new type of 2D

metallic ferromagnet with high Curie temperature. Nanoscale Horiz, 2018, 3: 335–341

Acknowledgements This work was supported by the National Key Research and Development Program of China (2017YFB0701600), the National Natural Science Foundation of China (11974197 and 51920105002), Guangdong Innovative and Entrepre-neurial Research Team Program (2017ZT07C341), China Postdoctoral Science Foundation (2018M631458), and the Bureau of Industry and Information Technology of Shenzhen for the 2017 Graphene Manufacturing Innovation Center Project (201901171523). The authors thank Runzhang Xu and Nannan Luo for helpful discussion.

Author contributions Zou X conceived the project. Gu Y performed the calculations. Gu Y, Zhang S and Zou X analyzed the data and co-wrote the paper. All authors discussed the results and commented on the manuscript.

Conflict of interest The authors declare that they have no conflict of interest.

Supplementary information Supplementary data can be found in the online version of the paper.

Yue Gu received his MSc degree from the School of Advanced Materials, Peking University Shenzhen Graduate School, in 2018. He is currently a PhD candidate at Tsinghua-Berkeley Shenzhen Institute (TBSI), Tsinghua University, under the supervision of Prof. Xiaolong Zou. His interest focuses on the theoretical simulations of magnetism and coupled spin in low-dimensional materials.

Xiaolong Zou received his PhD degree in physics from Tsinghua University, China, in 2011. After working as a research associate at Rice University, Houston, USA, he joined TBSI, Tsinghua University, as an assistant professor in 2016. His current research focuses on the theoretical description of the growth of 2D materials and their electronic, magnetic, optical, and catalytic properties.

层状$CoPS_3$中磁性的压力与载流子掺杂可控调节

顾越, 张树清, 邹小龙*

摘要 最近发现的层状铁磁材料吸引了研究者的广泛兴趣, 但是其有限的数量严重阻碍了进一步的发展. 作为一个更大的家族, 层状反铁磁材料为加深对基本磁性物理的理解和推动高性能自旋电子学的应用提供了一个出色的平台. 本文中, 我们选取了过渡金属磷三硫族化合物中代表性的反铁磁$CoPS_3$材料, 并通过系统的第一性原理计算证实压力或载流子掺杂可有效调控它的磁性. 特别地, 压力可以驱动其同构的Mott相变, 这与其他过渡金属磷三硫族化合物形成了鲜明的对比. 有趣的是, 压力和载流子掺杂都可以实现具有100%自旋极化率的铁磁半金属态, 研究人员长期寻求的这种特殊铁磁态有助于提高自旋电流的注入和检测效率. 此外, Mott相变伴随着$CoPS_3$中的瞬时自旋交叉, 这样的协同自旋交叉有利于实现快速响应的可逆电子设备, 如数据存储设备、光学显示器和传感器等. 我们还进一步对铁磁半金属性及自旋交叉的机理进行了深入的分析. 本文所预测的$CoPS_3$材料的可调磁性、铁磁半金属性和自旋交叉, 为各种功能设备的设计提供了广阔的空间.

